THE ASTROPHYSICAL JOURNAL, 483:136–147, 1997 July 1

THE STABILITY OF RADIATIVELY COOLING JETS. II. NONLINEAR EVOLUTION

JAMES M. STONE[1] AND JIANJUN XU[2]
Department of Astronomy, University of Maryland, College Park, MD 20742
AND
PHILIP E. HARDEE[3]
Department of Physics and Astronomy, University of Alabama, Tuscaloosa, AL 35487
Received 1996 June 11; accepted 1997 January 20

ABSTRACT

We use two-dimensional time-dependent hydrodynamical simulations to follow the growth of the Kelvin-Helmholtz (K-H) instability in cooling jets into the nonlinear regime. We focus primarily on asymmetric modes that give rise to transverse displacements of the jet beam. A variety of Mach numbers and two different cooling curves are studied. The growth rates of waves in the linear regime measured from the numerical simulations are in excellent agreement with the predictions of the linear stability analysis presented in the first paper in this series. In the nonlinear regime, the simulations show that asymmetric modes of the K-H instability can affect the structure and evolution of cooling jets in a number of ways. We find that jets in which the growth rate of the sinusoidal surface wave has a maximum at a so-called resonant frequency can be dominated by large-amplitude sinusoidal oscillations near this frequency. Eventually, growth of this wave can disrupt the jet. On the other hand, nonlinear body waves tend to produce low-amplitude wiggles in the shape of the jet but can result in strong shocks in the jet beam. In cooling jets, these shocks can produce dense knots and filaments of cooling gas within the jet. Ripples in the surface of the jet beam caused by both surface and body waves generate oblique shock "spurs" driven into the ambient gas. Our simulations show these shock "spurs" can accelerate ambient gas at large distances from the jet beam to low velocities, which represents a new mechanism by which low-velocity bipolar outflows may be driven by high-velocity jets. Rapid entrainment and acceleration of ambient gas may also occur if the jet is disrupted.

For parameters typical of protostellar jets, the frequency at which K-H growth is a maximum (or highest frequency to which the entire jet can respond dynamically) will be associated with perturbations with a period of ~ 200 yr. Higher frequency (shorter period) perturbations excite waves associated with body modes that produce internal shocks and only small-amplitude wiggles within the jet. The fact that most observed systems show no evidence for large-amplitude sinusoidal oscillation leading to disruption is indicative that the perturbation frequencies are generally large, consistent with the suggestion that protostellar jets arise from the inner regions ($r < 1$ AU) of accretion disks.

Subject headings: galaxies: jets — hydrodynamics — instabilities — ISM: jets and outflows — MHD

1. INTRODUCTION

Some of the best studied examples of astrophysical jets are observed at optical wavelengths. Examples include both protostellar (Herbig-Haro) jets (Edwards, Ray, & Mundt 1993; Ray 1996) and jets from some types of active galactic nuclei, e.g., Seyfert galaxies. Optical jets make excellent laboratories for studying the hydrodynamics of collimated outflows for several reasons: (1) they are amenable to high-resolution imaging both by ground-based adaptive optics systems and the space-based *Hubble Space Telescope* (*HST*), and (2) in most cases, the optical radiation arises from forbidden emission lines, which allows spectroscopic studies to be used to determine both the kinematics and the physical properties (e.g., density, temperature, etc.) of the line-emitting gas.

Perhaps the most striking images of optical jets are provided by recent *HST* observations of several protostellar systems. With the high spatial resolution of *HST*, structures within the jet are resolved, which allows direct study of the internal dynamics of the jet beam in addition to studies of the effect of the jet on its surrounding ambient gas. In three systems, HH 30 (Stapelfeldt et al. 1997; Ray et al. 1997), HH 111 (Reipurth et al. 1997), and HH 34, the jet appears as a continuous but knotty band of emission near the source. In each system, however, the jet is neither perfectly straight (e.g., shows low-amplitude long-wavelength sinusoidal oscillations) nor perfectly symmetric (e.g., contains knots and filaments of emission that are not distributed symmetrically with respect to the center of the jet). *HST* images of the HH 47 jet (Heathcote et al. 1996) reveal an even more complex flow in this system. The jet is very filamentary and appears to undergo large-amplitude bends before terminating in a classic Mach disk and bow shock structure at the head of the jet. Associated with the kinks and bends in the HH 47 jet are Hα-emitting shock spurs driven into the ambient gas.

While it is obvious that images of more distant extragalactic jets will not reveal as much detail as those of nearby protostellar jets, recent observations of Seyfert jets have discovered complex and puzzling asymmetric structures. Perhaps the best example is the helical jet in NGC 4258 (Cecil, Wilson, & Tully 1992) in which three tightly wrapped strands appear to spiral around one another for two full cycles before dispersing. Kinematics of the jet suggest that the jet material moves along the strands, so that the helical

[1] jstone@astro.umd.edu.
[2] xu@astro.umd.edu.
[3] hardee@venus.astr.ua.edu.

pattern is not a fixed structure carried outward by the flow. These observations led Cecil et al. to speculate that fluid dynamical instabilities in the shear layer between the jet and ambient gas might be responsible for forming the strands.

The observations suggest several possibilities for the formation of complex structure in jets:

1. A possibility suggested by both kinematic and morphological data of protostellar jets is that they are time variable in velocity, perhaps owing to variability in the underlying driving mechanism. Fluctuations in the jet velocity that exceed the internal sound speed result in the formation of internal shocks (Raga & Kofman 1992), and hydrodynamic simulations of the propagation of pulsed jets show that these shocks develop quickly near the jet nozzle and produce a layer of postshock cooling gas in the jet that can account for many of the observed properties of the observed emission knots (Hartigan & Raymond 1993; Stone & Norman 1993b; Gouviea dal Pino & Benz 1994; Biro & Raga 1994).

2. Inhomogeneities in the external medium can affect jet propagation and produce complex structure. For example, Stone & Norman (1994) investigated the effect of a transverse density gradient on the propagation of a cooling jet, and, more recently, Raga & Cantó (1996) have considered the effect of a jet/cloud impact with possible application to the HH 110 system (Reipurth, Raga, & Heathcote 1996). This work was preceded by even earlier work that examined the interaction of extragalactic jets with clouds in the interstellar/intergalactic medium (Wilson 1988; Norman & Balsara 1993; Clarke 1993).

3. It has been suggested that precession of the accretion disk can result in large reorientations in the direction of propagation of a jet, which produces either discrete knots that follow diverging paths (Raga & Biro 1993) or a more continuous oscillatory pattern (Raga, Cantó, & Biro 1993; Biro, Raga, & Cantó 1995).

4. Finally, as first suggested by Bührke, Mundt, & Ray (1988; hereafter BMR), the growth of Kelvin-Helmholtz (K-H) instabilities in the jet can result in the formation of structure (see also Bodo et al. 1994; Massaglia et al. 1992). BMR suggested that waves associated with the pinch mode of the K-H instability may result in knots in the jet, although it now appears that observations of the spacing and proper motion (see, e.g., Eislöffel & Mundt 1994) of the observed knots favors the internal working surface interpretation. Nevertheless, extensive studies of the K-H instability relevant to extragalactic jets (see Birkinshaw 1991 for a review) reveals that supermagnetosonic jets are always unstable. Thus, asymmetric modes of the K-H instability may still play a significant role in the development of structure.

An important property of optical jets is that in most systems (e.g., both protostellar and optical Seyfert jets), the optical emission results in a loss of internal energy from the gas, i.e., the jet is radiatively cooled. If the cooling time of the gas is comparable to or less than the dynamical flow time, the loss of internal energy via cooling can substantially alter the dynamics of cooling jets in comparison to adiabatic jets. Thus, although the stability properties of "adiabatic" extragalactic jets are relatively well studied, such is not the case for cooling jets. Both Hunter & Whitaker (1989) and Massaglia et al. (1992) showed that radiative cooling can significantly modify the K-H instability.

In a companion paper (Hardee & Stone 1997; hereafter Paper I), we presented a comprehensive linear stability analysis of "cooling" jets. In Paper I, the growth of K-H symmetric pinch and asymmetric sinusoidal modes were calculated in the linear regime for several Mach numbers over a broad range of perturbation frequencies. Not surprisingly, we found that the growth rates and wavelengths of the K-H modes in the cooling jet differed substantially from those of the adiabatic jet. Depending on the slope of the cooling curve near the equilibrium temperature, modes could either be damped or amplified relative to the adiabatic limit. Fluid displacement surfaces associated with various surface and body waves associated with the pinch and sinusoidal modes were also calculated in order to predict structures in the nonlinear regime. This analysis indicated that low-frequency perturbations should be the most effective at disrupting the jet. In this paper, we extend the analysis of Paper I by following the growth of K-H unstable waves into the nonlinear regime using time-dependent hydrodynamical simulations. Our goal is to study both the saturation and structure of K-H modes in the nonlinear regime and to provide direct comparison to observations.

There is an important difference between our present numerical studies of the K-H instability in jets and numerical studies of "precessing" jets, even though the tools and techniques of both studies are otherwise very similar. First, it is important to emphasize that the K-H instability studied here is a fluid dynamical phenomenon that can be captured only with a full hydrodynamical treatment of the evolution of a jet. Despite the fact that the jets studied here are highly overdense with respect to their surroundings, their dynamics is not well approximated by ballistic particles (an approximation that is valid only for jets that are more than 100 times denser than their surroundings). Moreover, in models of precessing jets, the direction of propagation of the jet is assumed to undergo large-amplitude variations, which result in transverse velocities at the jet nozzle *that exceed the sound speed*. Thus, the body of the jet cannot respond dynamically, and transverse shocks whose properties are determined by the assumed amplitude and frequency of the driving motion result. In the work presented here, we provide only small-amplitude, *linear* perturbations to the transverse motion of the jet. Typically, the transverse velocities induced by such perturbations are only a few percent of the sound speed; thus, the perturbations will result in linear-amplitude transverse sound waves in the jet. These linear waves are then amplified by the shear at the jet-ambient medium interface, ultimately producing large-amplitude, nonlinear phenomena occurring far downstream of the nozzle, and whose properties reflect the dynamical properties of the resonant cavity that is formed by the jet beam. The difference between the hydrodynamical evolution of nonlinear and linear amplitude perturbations applied at the jet nozzle is both substantial and essential. Moreover, it seems certain that astrophysical jets will be subject to linear amplitude perturbations owing to a variety of effects (nonlinear amplitude perturbations are less likely); thus, K-H modes should be relevant to all jets to some degree. Of course, in a real system, K-H instabilities may occur in addition to jet velocity variations (pulsing) and perhaps even large-scale readjustments to the jet direction. Thus, detailed models of specific observations may require the addition of more than one of these effects.

Finally, we note that for the reasons discussed in Paper I, we confine the analysis in this paper to two-dimensional slab jets. By adopting a slab geometry, we are able to study the asymmetric sinusoidal mode of the jet, as well as the symmetric pinch mode. While the pinch mode has been studied as a possible source of emission knots in protostellar jets (BMR; Massaglia et al. 1992), it is the sinusoidal mode that can result in wiggles, bends, and jet disruption. Moreover, the linear analysis shows that the sinusoidal mode on the slab jet is a direct analog of the helical mode on a three-dimensional jet of circular cross section. By confining our studies to two dimensions, we are able to perform a numerical parameter survey more efficiently. We will study the linear stability properties and nonlinear evolution of a three-dimensional cooling jet in a future communication.

The organization of this paper is as follows. In the following section, we describe our numerical methods for evolving the equations of hydrodynamics including optically thin radiative cooling. In § 3, we compare our numerical results with the analytic analyses of Paper I in the linear regime and describe the evolution of K-H unstable jets in the nonlinear regime for a variety of parameters. In § 4, we compare our results to observations of protostellar jets, and in § 5, we conclude.

2. NUMERICAL METHODS

2.1. *Hydrodynamical Algorithms*

The dynamical evolution of a supersonic jet is given by solutions to the mass, momentum, and total energy conservation equations:

$$\frac{\partial \rho}{\partial t} + \nabla \cdot (\rho \boldsymbol{v}) = 0 , \tag{1}$$

$$\frac{\partial \rho \boldsymbol{v}}{\partial t} + \nabla \cdot (P + \rho \boldsymbol{v}\boldsymbol{v}) = 0 , \tag{2}$$

$$\frac{\partial \rho E}{\partial t} + \nabla \cdot (P\boldsymbol{v} + \rho \boldsymbol{v} E) = -n^2\Lambda + nH , \tag{3}$$

where ρ is the mass density, $\boldsymbol{v}$ is the velocity vector, P is the pressure tensor with diagonal components p, and $E = (\gamma - 1)^{-1} p/\rho + 0.5(\boldsymbol{v} \cdot \boldsymbol{v})$ is the total specific energy (here, we use $\gamma = 5/3$). The two terms on the right-hand side of equation (3) account for energy losses due to optically thin radiation and heating of the gas, respectively. In these terms, Λ is the per particle cooling rate, H is the heating rate, and $n = \rho/\bar{m}$ is the number density of particles of mean mass $\bar{m}$. We adopt $\bar{m} = 1.4 m_{\rm H}$, where $m_{\rm H}$ is the mass of the hydrogen atom.

In order to generate solutions to equations (1)–(3), we use an implementation of the piecewise parabolic method (PPM) to evolve the left-hand side of equations (1)–(3) numerically. Following standard practice, we operator-split the solution of the right-hand side of equation (3) into a separate step. We use a fully implicit backward Euler scheme combined with Newton-Raphson iterations to advance the nonlinear heating and cooling terms. This ensures that our numerical scheme is stable even when the cooling time is much less than the dynamical time. The exact form adopted for Λ and H is described below.

For highly supersonic flows, we have found the accuracy of the numerical evaluation of the heating and cooling rates is improved by solving an internal energy equation along with the other conservation laws. In hypersonic flows, the total energy E is dominated by the kinetic energy E_k. The small difference between two large numbers ($E - E_k$) leads to round-off errors in the calculation of the temperature, which is proportional to $E - E_k$. In most cases, e.g., studies of propagating jets, this error does not affect the dynamics since (1) it is extremely small (of order the machine word length) and (2) it occurs only where the pressure is negligible. However, in this work, we wish to study the dynamical evolution of unstable jets that are initially in a delicate pressure equilibrium with a low-density ambient medium and in which the net cooling rate (which is a strongly nonlinear function of temperature) is $n^2\Lambda - nH = 0$. In this case, round-off errors can introduce perturbations that are amplified by the net cooling rate and that can eventually overwhelm those introduced at the jet nozzle. Thus, we improve the consistency of the temperature evolution by solving an internal energy equation

$$\frac{\partial e}{\partial t} + \boldsymbol{v} \cdot \nabla e = -\frac{P}{\rho} \nabla \cdot \boldsymbol{v} , \tag{4}$$

using fluxes evaluated numerically from the PPM algorithm (Bryan et al. 1995), where e is the internal energy, and then use e to compute the temperature in the evaluation of the cooling terms. The total energy E is still used to evolve the hydrodynamics. Only with this extension were we able to hold the initial equilibrium state for many dynamical times if it was not perturbed.

In order to follow the mixing of jet and ambient material, we evolve a Lagrangian tracer variable that we term the "color" C of the fluid. The evolution of C is described by the additional conservation law

$$\frac{\partial \rho C}{\partial t} + \nabla \cdot \rho C \boldsymbol{v} = 0 , \tag{5}$$

which is updated along with equations (1)–(3) using PPM. Initially, the jet material is labeled by $C = 1$, while the ambient gas is labeled $C = 0$. As the jet evolves, the ambient and jet gases mix, which results in regions with $0 < C < 1$.

2.2. *Cooling Rates*

An important aspect of the numerical simulation of the dynamical evolution of cooling jets is an accurate treatment of the microphysical heating and cooling rates. In a series of papers that studied the propagation of protostellar jets, Stone & Norman (1993a, 1993b, 1994) adopted a nonequilibrium ionization formalism to improve the accuracy of the cooling terms. This method required solving an ionization and recombination rate equation for neutral hydrogen in addition to the conservation laws equations (1)–(3) in order to compute the ionization fraction of the gas. Cooling due to both the ionized and neutral components of the medium could then be calculated self-consistently along with the dynamics. In Stone & Norman (1993a), it was shown through the use of a test problem based on the overstability of radiative shocks that this nonequilibrium treatment of the cooling rate led to significantly improved estimates for the total cooling rates in comparison to cooling based on the assumption of complete ionization. However, incorporating a time-dependent ionization fraction into the linear stability analysis of a cooling jet is intractable. Thus, in Paper I, the cooling rate was assumed to be given by equi-

librium cooling curves in order to study the stability properties of the cooling jet. Two separate cooling curves were adopted in Paper I: one appropriate to interstellar gas, and one to photoionized gas with reduced metallicity. Since in Paper I we consider only linear amplitude perturbations in the cooling rate away from the equilibrium state, each of these cooling functions was represented by a power law in the neighborhood of the equilibrium temperature.

In this paper, we adopt the same assumptions as used in Paper I in order to allow direct comparison of the results in the linear regime. Therefore, here the per particle cooling rate Λ is determined by one of the two cooling curves adopted in Paper I. However, because we study nonlinear effects in this paper, we do not represent the cooling curves as power laws in the neighborhood of the equilibrium temperature, and instead we implement the full nonlinear curve over a wide range of temperature. Both of the cooling curves used in the simulations are plotted in Figure 1. Each simulation uses either the cooling curve for interstellar gas calculated by Dalgarno & McCray (1972; hereafter DM) plotted in Figure 1*a* or the curve described by MacDonald & Bailey (1981; hereafter MB) for photoionized gas of reduced metallicity plotted in Figure 1*b*. In both cases, the heating rate H is then determined by the requirement that the jet be in equilibrium initially, i.e., the right-hand side of equation (3) is zero.

2.3. *Initial and Boundary Conditions*

The simulations presented in this paper are all computed using Cartesian coordinates. We vary the size of the computational domain in the axial direction depending on the Mach number of the jet and the perturbation frequency in order to ensure that many wavelengths of the most unstable mode can be captured. Typically, the grid is of size $-10R_{jt} \leq Y \leq 10R_{jt}$ in the transverse direction and $0 \leq X \leq 100 - 400R_{jt}$ in the axial direction, where R_{jt} is the radius of the jet. In different simulations, we use from 200 to 600 zones in the transverse direction, with from 10 to 40 zones across a jet diameter. To allow the maximum resolution within the jet beam, nonuniform-sized zones are used beyond $|Y| > 2R_{jt}$. In the axial direction, 400–800 zones are used. Outflow boundary conditions are used along the outer Y boundaries, along the outer X boundary, and along the inner X boundary for $|Y| > 1R_{jt}$. For $|Y| \leq 1R_{jt}$ along the inner X boundary, inflow boundary conditions are used with the variables held fixed at the values appropriate to the initial equilibrium structure of the jet.

We initialize the jet across the entire mesh for $|Y| \leq R_{jt}$, i.e., an equilibrium jet as opposed to a propagating jet. Initially, the jet is assumed to be perfectly collimated with density n_{jt}, velocity v_{jt}, and temperature T_{jt}. The background medium is stationary, with a uniform density n_{ex} and with a pressure that matches that of the jet so that $T_{ex} = (n_{jt}/n_{ex})T_{jt}$. Motivated by recent observations of various protostellar jets (see, e.g., Ray 1996), we adopt as typical values for a protostellar jet a radius $R_{jt} = 2.5 \times 10^{15}$ cm; external Mach number $M_{ex} = v_{jt}/a_{ex} = 5$ or 20, where a_{ex} is the sound speed in the external medium; number density $n_{jt} = 600$ cm^{-3}; and temperature $T_{jt} = 1000$ K. The ambient interstellar gas has a number density $n_{ex} = 60$ cm^{-3}, temperature $T = 10{,}000$ K, and sound speed $a_{ex} = 1.18 \times 10^6$ cm s^{-1}. This implies we are studying overdense jets, with $n_{jt}/n_{ex} = 10$. There are two important timescales in the simulations. The first is the dynamical or sound crossing time $\tau \equiv R_{jt}/a_{jt}$, which for the parameter value listed above is equal to 213 yr. The second is the grid crossing time

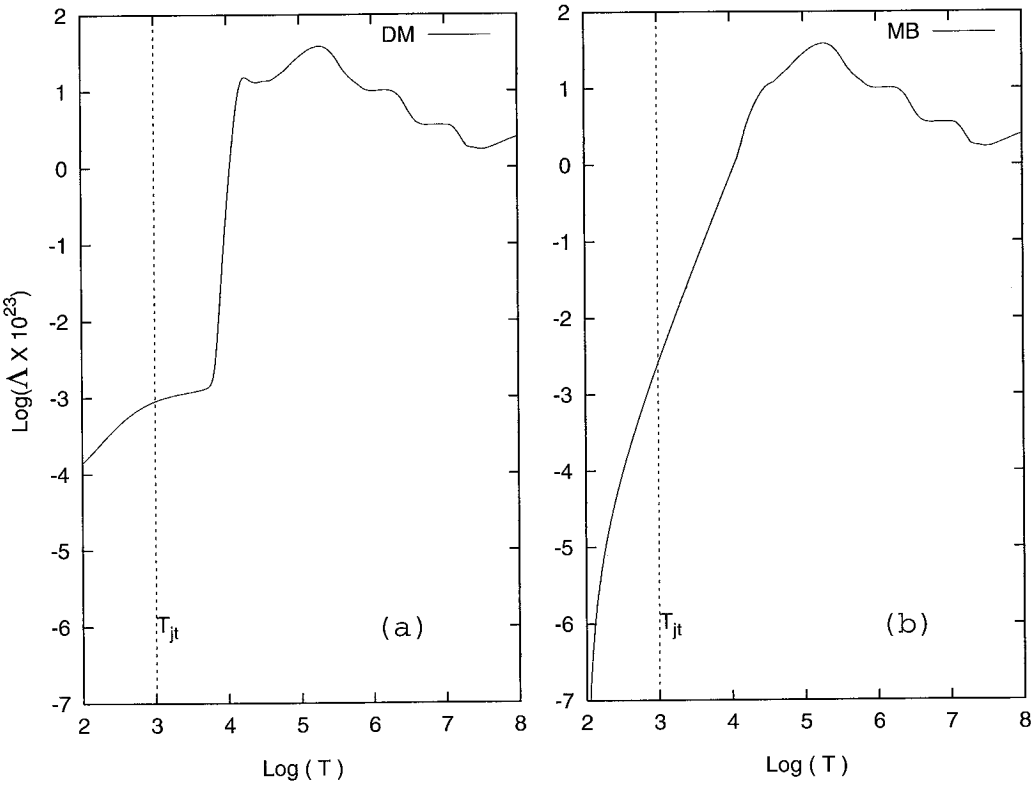

FIG. 1.—Per particle cooling rates used in the simulations for the (*a*) Dalgarno & McCray (1972; DM) cooling curve, and (*b*) MacDonald & Bailey (1981; MB) cooling curve.

$t_c \equiv L_{\rm grid}/v_{\rm jt}$, where $L_{\rm grid}$ is the axial length of the computational domain. This latter timescale varies with the Mach number of the jet and the size of the grid; each simulation is followed for several t_c so that the jet reaches a quasi-steady structure in the nonlinear regime.

As discussed in Paper I, in this study we focus on the development of K-H modes in jets that are overdense with respect to their surroundings. Because we must study pressure-matched jets in order to begin with an equilibrium state, this implies the jet beam is cooler than its surroundings. Physically, our models may represent a dense jet beam embedded in a hotter and less dense cocoon that has been swept up by the bow shock associated with the leading surface. Dense molecular outflows that are often observed to be associated with protostellar jets (Reipurth & Cernicharo 1995) may surround the cocoon. There is substantial observational evidence that protostellar jets are overdense with respect to their surroundings (see, e.g., Ray 1996). The fact that they remain well collimated for lengths that are much larger than their radii argues they must be in pressure equilibrium with their surroundings (or they would expand rapidly). Finally, the kinematic model of a dense jet embedded in a less dense cocoon that is in turn ensheathed by a very dense and cold molecular gas is consistent with detailed observation of a number of systems, including HH 111 (Nagar, Vogel, & Stone 1996).

In order to excite K-H modes, at time $t = 0$, a sinusoidal perturbation of the transverse velocity is turned on at the nozzle ($x = 0$). (As a test of our numerical methods, we have verified that the code will hold the initial equilibrium state indefinitely if no perturbation is applied to the jet.) The amplitude of the perturbation is set to $u_y = \theta_{\rm jt} M_{\rm ex} a_{\rm ex}$, where $\theta_{\rm jt}$ is varied from 0.0025 to 0.01 for different driving frequencies. The velocity perturbation is of the form

$$u_y(x = 0) = \theta_{\rm jt} M_{\rm ex} a_{\rm ex} \sin(\omega t) . \quad (6)$$

Because the wavelength of the most unstable modes varies with perturbation frequency, the axial length of the grid is chosen to ensure the grid will encompass several unstable wavelengths.

3. RESULTS

3.1. *Evolution in the Linear Regime: The Asymmetric Surface Wave*

A linear analysis of the stability of the adiabatic slab jet reveals that the dominant K-H instable waves in a thermal pressure–confined jet are the asymmetric surface and symmetric and asymmetric internal body waves (see, e.g., Hardee & Norman 1988). In general, the same is true for the cooling slab jet; however, the growth rates and wavelengths of unstable modes are strongly affected by the effect of cooling (Paper I), and at high frequency, even the symmetric surface wave can be important on the cooling jet. As an important consistency check between the analytic calculations presented in Paper I and the numerical simulations presented here, we have compared the growth rates of K-H modes computed using both methods in the linear regime. We concentrate on the asymmetric surface wave, since in the frequency domain we are studying, the surface wave dominates the internal body waves. Moreover, we study the response of the jet to different driving frequencies, i.e., we fix ω and study spatial instabilities. While the temporal growth rate can contribute to the total spatial growth rate (see, e.g., Zhao et al. 1992), in the linear regime the contribution is negligible.

We have found a straightforward and accurate way to measure the linear growth rate of waves in our hydrodynamical simulations based on evolution of the "color" variable C that labels the jet and ambient gas. Perturbations induced at the jet nozzle result in a transverse velocity field that can be written as

$$u_y(x, t) = \theta_{\rm jt} M_{\rm ex} a_{\rm ex} \exp\{k_I x\} \sin(\omega t) , \quad (7)$$

where k_I is the imaginary part of the wavenumber. For a uniform ambient gas, the displacement amplitude of the surface wave is therefore given by (see, e.g., eq. [11] in Hardee, Norman, & Clarke 1994)

$$A = A_0 \exp\{k_I x\} . \quad (8)$$

A schematic illustration of the growth of the surface wave is given in Figure 2. The locus of points marking the maximum transverse displacement of the jet at each axial location should therefore follow the exponential curve described by equation (8). We use the color variable to measure this exponential envelope in the following manner. The jet is evolved for many dynamical times, and the maximum transverse amplitude that the jet material reached throughout the evolution (found by plotting the envelope that encloses material with $C = 1$) at each axial position is measured. We find that a plot of this amplitude versus axial distance from the nozzle follows the exponential envelope illustrated in Figure 2 extremely well. Figure 3 demonstrates this procedure for a simulation of a Mach 5 cooling jet computed using the MB cooling curve and perturbed at a frequency of $\omega R_{\rm jt}/a_{\rm ex} = 0.5$.

In order to compare the analytic and numerical growth rates at a variety of frequencies and jet parameters, we have performed numerical simulations at $\omega R_{\rm jt}/a_{\rm ex} = 0.2$, 0.5, 2.0, and 5.0 for both Mach 5 and Mach 20 jets computed with an adiabatic equation of state, DM cooling, and MB cooling. The parameters of each of these test simulations are listed in Tables 1 and 2. In these tables, an upper limit to the perturbation wavelength is given by $\lambda_{\rm max} = 2\pi u/\omega R_{\rm jt}$. The true perturbation wavelength depends on the wave propagation speed and is different from the above estimate by the factor v_w/u. The linear analysis indicates that to zeroth-order a reasonable estimate of the wave propagation speed is $v_w = [\eta^{1/2}/(1 + \eta^{1/2})]u$, where $\eta \equiv \rho_{\rm jt}/\rho_{\rm ex}$. A more accurate determination requires referral to the complete dispersion relation solutions given in Paper I. We choose $\theta_{\rm jt}$ to be small, but since the displacement amplitude of the surface

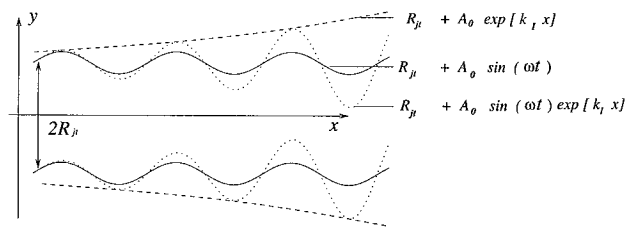

FIG. 2.—Illustration of the growth of the fundamental surface wave. The solid sinusoidal line denotes the perturbation applied to the jet beam. The dotted line represents the effect of the exponential growth of the amplitude of the perturbation. The dashed line denotes the envelope of the maximum amplitude of the transverse position of the jet beam at each axial location.

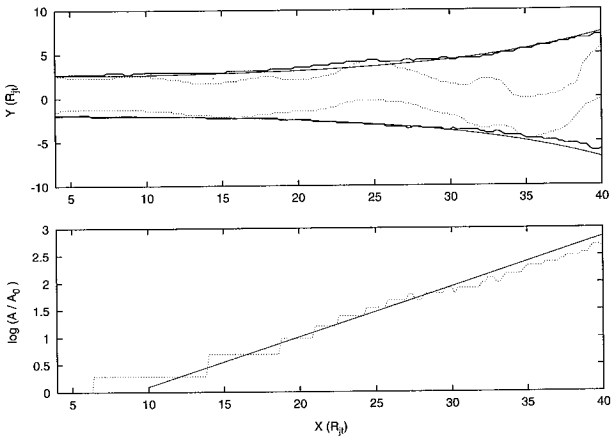

FIG. 3.—Illustration of our procedure for measuring the growth rate of K-H modes from the numerical simulations. *Top*: The dotted line shows the isocontour of $C = 1$ at a late time in a simulation of a Mach 5, DM cooling jet to demonstrate the typical structure of the jet beam. The bold line shows the maximum displacement of the jet beam (defined by the $C = 1$ isocontour) throughout the entire simulation. The solid line is an exponential fit to the maximum displacement. *Bottom*: Fit of the amplitude of the jet displacement.

wave is proportional to $\theta_{jt}u/\omega$, at high frequencies, θ_{jt} is increased in order to resolve the transverse displacement.

In Figures 4 and 5, we plot the growth rates of the surface waves measured from the numerical simulations (plotted as points) with the analytic results of Paper I (plotted as lines) for the Mach 5 and Mach 20 jets, respectively. The top panel in each figure compares the analytical and numerical results for an adiabatic jet, the middle panel for a non-adiabatic jet computed with the DM cooling curve, and the bottom panel for a nonadiabatic jet computed with the MB cooling curve.

From Figure 4, it can be seen that the growth rate of the sinusoidal mode surface wave measured from the numerical simulations agrees very well with the analytic growth rate calculated in Paper I for low frequencies ($\omega R_{jt}/u \leq 0.4$; $\omega R_{jt}/a_{ex} \leq 2.0$). For the adiabatic and MB cooling jet, the growth rate of the sinusoidal mode body waves (plotted as dashed lines) exceeds that for the surface wave (plotted as a solid line) at high frequencies. Our numerically measured

TABLE 1

PARAMETERS OF SIMULATIONS OF $M = 5$ JETS

ω	$\omega R_{jt}/u$	λ^a_{max}/R_{jt}	X^b/λ_{max}	$N_{jt}{}^c$	θ_{jt}
0.2.....	0.04	157.0	2.5	10	0.01
0.5.....	0.1	63.0	3.2	20	0.02
2.0.....	0.4	15.7	3.8	40	0.03
5.0.....	1.0	6.3	4.8	40	0.075

[a] Upper limit to perturbation wavelength.
[b] Length of the computational domain.
[c] Number of zones across the jet diameter.

TABLE 2

PARAMETERS OF SIMULATIONS OF $M = 20$ JETS

ω	$\omega R_{jt}/u$	λ_{max}/R_{jt}	X/λ_{max}	N_{jt}	θ_{jt}
0.2.....	0.01	630.0	1.9	20	0.001
0.5.....	0.025	250.0	2.0	20	0.0025
2.0.....	0.1	63.0	6.3	20	0.005
5.0.....	0.25	25.0	8.0	40	0.01

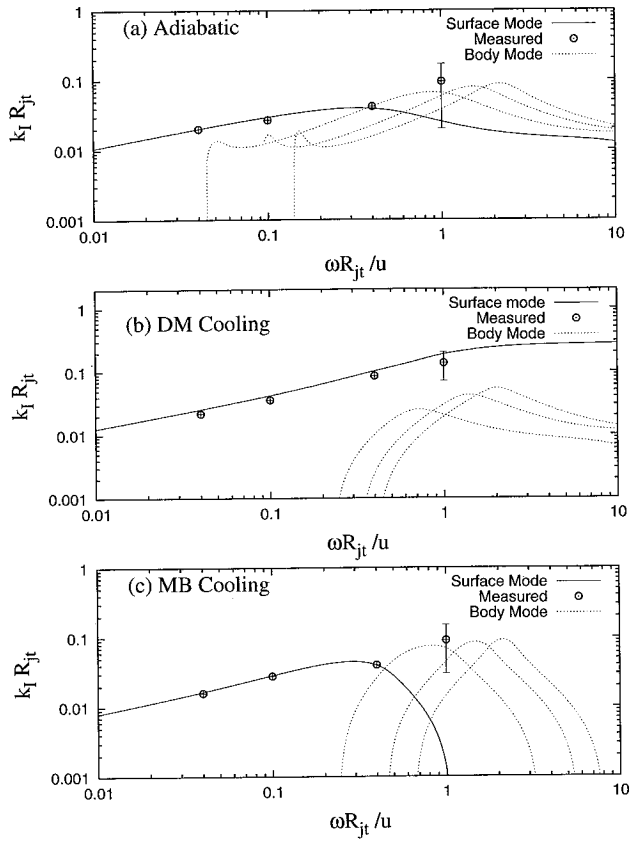

FIG. 4.—Comparison of the analytic and numerical growth rates in the linear regime for a Mach 5 jet. In each panel, the solid line is the growth rate of the fundamental surface wave as calculated by the linear analysis in Paper I, while the dashed lines are the growth rates of the fundamental and first two body modes. Growth rates measured from the numerical simulations are plotted as points with error bars. *Top*: Comparison for an adiabatic jet. *Middle*: Comparison for a cooling jet computed with the DM cooling curve. *Bottom*: Comparison for a cooling jet computed with the MB cooling curve.

growth rate agrees well with the analytic growth rate of the body waves at high frequency ($\omega R_{jt}/u = 1$; $\omega R_{jt}/a_{ex} = 5$), although there is considerable error in the determination of the growth rate. This error results from the growth of multiple body waves in the jet, which makes measurement of the growth rate of the fastest growing wave difficult using the techniques described above and in Figure 3.

Inspection of Figure 5, which compares the numerical and analytical growth rates for waves in a Mach 20 jet, reveals similar trends. At low frequencies ($\omega R_{jt}/u \leq 0.1$; $\omega R_{jt}/a_{ex} \leq 2.0$), the numerical results agree very well with the analytic growth rate for the sinusoidal mode surface wave. At a higher frequency, $\omega R_{jt}/u = 0.25$ ($\omega R_{jt}/a_{ex} = 5.0$), the growth rate of the sinusoidal mode body waves exceeds that of the surface wave for the adiabatic and MB cooling jet, and our numerically measured rates agree well with the body wave growth rate. Note that by comparing Figures 4 and 5, it is evident that the growth rates, cutoff frequencies, and frequency of maximum growth all scale as the ratio of the Mach number between the Mach 5 and 20 jets as expected (Paper I).

These results confirm the linear prediction that the jet cannot respond to a driving frequency above about $\omega R_{jt}/a_{ex} \approx 2$ by the development of a large-amplitude surface wave distorting the entire jet. Instead, internal

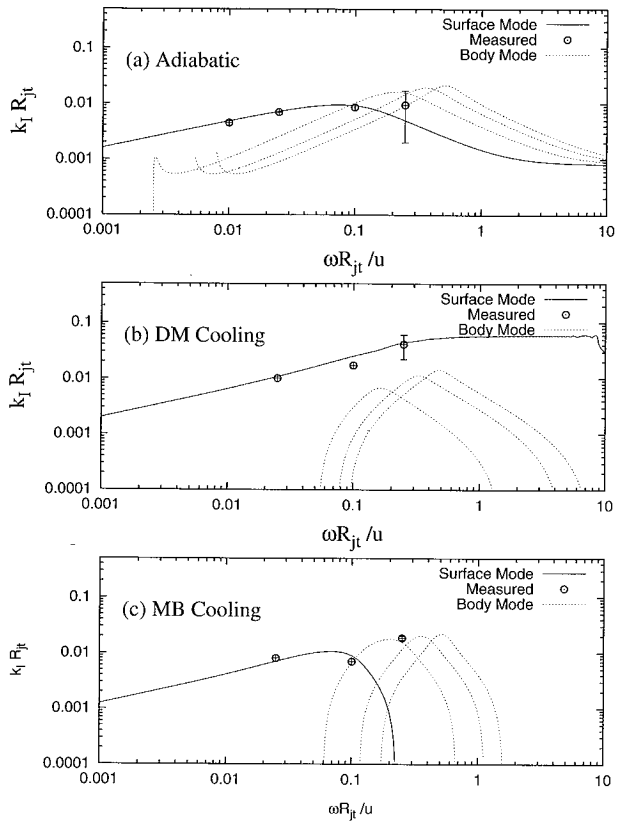

FIG. 5.—Same as Fig. 4 for a Mach 20 jet

waves can be generated at the corresponding short wavelength (e.g., behavior of the asymmetric surface mode shown in Fig. 5 in Paper I). Thus, the jet is dominated by internal waves from the faster growing body modes (adiabatic and MB cooling jets) or by internal waves from the cooling enhanced faster growing surface wave (DM cooling jet).

3.2. *Evolution in the Nonlinear Regime*

The primary purpose of this paper is to use numerical methods to follow the growth of K-H modes in cooling jets into the nonlinear regime and to study the structure in the saturated state. Because of the exponential growth of waves, the linear regime will be short lived in real systems; thus, the structure and morphology of observed jets should be best fitted by nonlinear hydrodynamical calculations. In the following subsections, we describe the properties of the nonlinear stage of the K-H instability observed in our simulations.

3.2.1. *The Asymmetric Surface Wave*

The linear analysis shows that the growth of the surface wave experiences a maximum at some intermediate frequency in both adiabatic and MB cooling jets (see Figs. 4 and 5). In the nonlinear regime, mode-mode coupling can excite perturbations at this frequency even if the jet is driven at a different rate. Since this frequency has the highest growth rate, in the nonlinear regime, jets can be dominated by structures at the accompanying wavelength. This maximally growing frequency is sometimes referred to as the "resonant" frequency (see, e.g., Ferrari, Turssoni, & Zaninetti 1981; Hardee 1987).

To study the nonlinear response of the surface wave and investigate perturbations induced by mode-mode coupling, we have performed low-resolution simulations (10 zones across a jet diameter) of Mach 5 adiabatic (Ad), MB cooling (MB), and DM cooling (DM) jets driven at a relatively high frequency of $\omega R_{jt}/u = 1.0$. In each simulation, the computational domain has dimensions $0 \le X \le 400R_{jt}$, and $-20R_{jt} \le Y \le 20R_{jt}$, and a numerical resolution of 200×400 grid points. By using low numerical resolution, we artificially suppress the growth of body waves and therefore enhance the role of the surface wave in determining jet structure. The result is shown in Figure 6 (Plate 4), which presents gray-scale images of the logarithm of the density in each jet at a dynamical time of $t = 100\tau$ (note the grid crossing time for these simulations is $t_c = 80\tau$). From Figure 4, it is clear that the adiabatic jet has a weak maximum in the growth rate at $\omega R/u \approx 0.3$, the DM cooling jet lacks any resonant frequency, and the MB cooling jet has a strong maximum in the growth rate at $\omega R/u \approx 0.3$. The structures observed in Figure 6 seem to reflect the relative strength of the maximum in the growth rate. For example, the adiabatic jet shows a weak sinusoidal pattern, the DM cooling jet has a complex and time-dependent structure that is not dominated by any one frequency, and the MB cooling jet develops a large amplitude sinusoidal oscillation that undergoes exponential growth from the nozzle until the jet is disrupted near $r = 300R_{jt}$. The quasi-steady oscillation pattern has a wavelength $\lambda \approx 26R_{jt}$ that corresponds to a linear perturbation frequency $\omega R_{jt}/u \approx 0.2$ despite the fact that perturbation frequency is much higher. This result is consistent with growth near the resonant frequency $\omega R_{jt}/u = 0.29$ and wavelength $\lambda = 17.5R_{jt}$ predicted by the linear analysis but suggests that longer wavelengths that grow at less than the maximum growth rate can come to dominate as they can attain larger amplitudes. These results once again confirm the linear prediction that the jet cannot respond to a driving frequency above about $\omega R_{jt}/a_{ex} \approx 2$ by the development of a large-amplitude surface wave at the corresponding short wavelength.

In order to investigate the internal dynamics of the jet beam and asymmetric surface wave in more detail, we have calculated the evolution of Mach 5 adiabatic, DM cooling, and MB cooling jets driven at a frequency $\omega R_{jt}/u = 0.4$ (near the maximum growth rate of the surface wave) and using a computational domain of size $0 \le X \le 60R_{jt}$ by $-5R_{jt} \le Y \le 5R_{jt}$ and 200×400 grid points (giving 40 zones across a jet diameter). We plot gray-scale images of the logarithm of the density at dynamical time $t = 15\tau$ in Figure 7 (Plate 5) (the grid crossing time is $t_c = 12\tau$). In each case, internal structure associated with sinusoidal oscillation grows strongly, forming a sequence of opposing shocks in the jet. The perturbation frequency of $\omega R_{jt}/u = 0.4$ lies below the resonant frequencies of the body waves and the linear analysis predicts asymmetric surface mode wavelengths given by $\lambda/R_{jt} = 13.1$ (Ad), 14.3 (DM), and 12.8 (MB) compared to the observed 13.3 (Ad), 14.4 (DM), and 14.8 (MB), and with the exception of the MB cooling jet, the agreement is excellent. The linear analysis predicts comparable growth rates for the adiabatic and MB cooling jets and a significantly larger growth rate for the DM cooling jet. Note that the DM cooling jet appears to disrupt at a lesser distance, $\approx 45R_{jt}$, than the adiabatic and MB cooling jets. In the cooling jets, the postshock gas becomes very dense. The corrugations in the edge of the jet produce oblique shock spurs in the ambient gas oriented in a sequence of opposing steps. Interestingly, the knots them-

selves are subject to Rayleigh-Taylor instabilities and slowly break up at late times. We discuss knot formation in K-H unstable jets more fully in § 3.2.4.

3.2.2. *The Asymmetric Body Waves*

In order to study the nonlinear response of the body waves, we have performed high-resolution simulations (20 zones across a jet diameter) of Mach 5 adiabatic, MB cooling, and DM cooling jets driven at a relatively high frequency of $\omega R_{jt}/u = 1.0$. In each simulation, the computational domain has dimensions $0 \le X \le 200R_{jt}$ and $-5R_{jt} \le Y \le 5R_{jt}$ and a numerical resolution of 100×800 grid points. By using high numerical resolution, we can study the role of both body and surface waves in determining jet structure. The result is shown in Figure 8 (Plate 6), which presents gray-scale images of the density in each jet at a dynamical time of $t = 40\tau$. Note the similarity with the gross behavior from the low-resolution simulations shown in Figure 6 (i.e., the nearly symmetric adiabatic jet, the complex structure of the DM cooling jet, and the developing sinusoidal oscillation of the MB cooling jet). The developing oscillation of the MB cooling jet has the wavelength, $\lambda \approx 26R_{jt}$, observed in the lower resolution simulation (Fig. 6) at much longer dynamical time. These results confirm both (1) the linear prediction that the jet cannot respond to a driving frequency above about $\omega R_{jt}/a_{ex} \approx 2$ by the development of a large-amplitude surface wave at the corresponding short wavelength and (2) the validity of the low-resolution simulations.

The linear analysis predicts that at high frequencies, the growth of body waves is very rapid (see Figs. 3 and 4). Indeed, these high-resolution simulations of jets perturbed at high frequency show that the internal waves become nonlinear only a few wavelengths from the nozzle. At the driving frequency of $\omega R_{jt}/u = 1.0$, the linear analysis predicts that the wavelength of the asymmetric mode surface wave is $\lambda/R_{jt} = 5.62$ (Ad), 4.95 (DM), and 5.56 (MB) compared to the observed $\lambda/R_{jt} \approx 5.9$ (Ad), 6.3 (DM), and 6.1 (MB) at $< 50R_{jt}$. Note that the driving perturbation should excite the surface wave preferentially to the body waves, and this could overcome lower growth rates (cf. the adiabatic and MB cooling jet growth rates in Fig. 4); thus, the internal waves at axial distances of $< 50R_{jt}$ could be due to the surface wave. Differentiating between short-wavelength surface and body waves requires study of the internal structure. Beyond about $50R_{jt}$, the diagonal patterns in the images become more complex and indicate the presence of mixed surface and body waves. At these larger distances, we see evidence for ripples on the jet surface with separation (wavelength) in the range $\sim 6.3R_{jt}$–$4.7R_{jt}$ and internal oblique shock structures with separations (wavelengths) in the range $\sim 3R_{jt}$–$2R_{jt}$ on the order of one-half to one-third the separation of the ripples. We note that from the linear analysis a potential wavelength range for the asymmetric mode first body wave is $\lambda/R_{jt} < 5.4$ (Ad), 7.2 (DM), and 5.7 (MB), where the upper limit corresponds to the wavelength at maximum growth. The driving frequency is at a wavelength about 15% shorter. The linear analysis would also predict a potential wavelength range for the asymmetric mode second body wave to be $\lambda/R_{jt} > 3.17$ (Ad), 3.55 (DM), and 3.26 (MB), where the lower limit corresponds to maximum growth. The driving frequency is at a wavelength about 35% longer. Interestingly, the observed separations are shorter than would be expected from the linear analysis although well within the shorter wavelength growth rate range of these body waves. The observed patterns suggest that wave-wave coupling between the surface and body waves is not capable of prediction via a linear analysis.

At much lower frequencies, the body waves are predicted by the linear analysis to be stable (adiabatic jet) or damped (cooling jet). In Figure 9 (Plate 7), we plot gray-scale images of the density in Mach 20 adiabatic and DM cooling jets driven at a low frequency of $\omega R_{jt}/u = 0.025$. The computational domain in these simulations is of size $0 \le X \le 500R_{jt}$ by $-10R_{jt} \le Y \le 10R_{jt}$, and the numerical resolution is 200×400 grid points (giving 20 zones across a jet diameter). Each jet is shown at a time of $t = 25\tau$ (equivalent to one grid crossing time). Note that to reveal the transverse structures in more detail, we have distorted the images by reducing the axial distance by a factor of 4 relative to the transverse distance. When viewed with the correct aspect ratio, both jets appear essentially straight, although the oscillations achieve an amplitude on the order of the jet diameter. With the axial ratio as plotted, the images in Figure 9 should be representative of a Mach 5 jet, owing to Mach number scaling of growth rates and wavelengths.

Unlike jets perturbed at high frequency, jets perturbed at this low frequency have a long linear evolution phase. The long-wavelength oscillations have an observed $\lambda \approx 180R_{jt}$ (Ad) and $200R_{jt}$ (DM)—we have used the outermost oscillation to determine the wavelength—compared to the predicted $180R_{jt}$ (Ad) and $242R_{jt}$ (DM). The DM cooling jet is predicted by the linear analysis to have a growth rate $\approx 30\%$ larger than the adiabatic jet, and, in fact, the adiabatic jet remains relatively well collimated, whereas the DM cooling jet is disrupted and forms high-density knots associated with working surfaces in the ambient gas. The dense knots result from strong cooling effects (see § 3.2.4). In addition to these surface waves, both jets show evidence for internal oblique structures with wavelength in the range $40R_{jt}$–$50R_{jt}$ at axial distances in the range $100R_{jt}$–$200R_{jt}$. The linear analysis in Paper I shows that the first asymmetric body mode wave on the adiabatic jet would respond to this low-frequency perturbation with a wavelength of $84R_{jt}$, considerably longer than observed in the simulation, and that the first asymmetric body wave on the DM cooling jet is damped at this low frequency. However, we note that the observed wavelengths fall within the wavelength range $23R_{jt}$–$84R_{jt}$ on the adiabatic jet and $32R_{jt}$–$63R_{jt}$ on the cooling jet, where the short-wavelength limit is at the maximum growth rate and the long-wavelength limit is at the perturbation frequency or at the lowest frequency at which the wave is still unstable. Thus, we identify these internal structures with asymmetric body waves excited by the low-frequency perturbation.

In Figure 10 (Plates 8–10), we plot gray-scale images of the logarithm of the density and the color variable for simulations of Mach 5 adiabatic, DM cooling, and MB cooling jets. In each case, the jets are perturbed at a relatively low frequency of $\omega R_{jt}/u = 0.1$, and the simulations are extended until dynamical time $t = 200\tau$ (or 2.5 crossing times) when the jets have all reached a quasi-stationary state. We use a high-resolution grid consisting of 600×800 zones (20 zones across jet diameter) to resolve internal jet structure, with a computational domain of size $0 \le X \le 400R_{jt}$ by $-30R_{jt} \le Y \le 30R_{jt}$. The linear analysis in Paper I predicts that this frequency is below the body wave resonant

frequencies on the adiabatic jet and that the body waves are damped at this frequency on the cooling jets. The jets all show a long linear evolution phase and an overall sinusoidal pattern associated with the growth of surface waves. The long-wavelength oscillations have an observed $\lambda \approx 50R_{jt}$ (Ad), $52R_{jt}$ (DM), and $51R_{jt}$ (MB) compared to a calculated $46.7R_{jt}$ (Ad), $59.3R_{jt}$ (DM), and $49.1R_{jt}$. The surface wave grows to large amplitude at large distances from the nozzle and disrupts the jet. Shock spurs driven into the ambient gas by the sinusoidal jet oscillations are evident.

In addition to the surface wave, there are oblique structures within the jets. In the cooling jets, these structures are manifested primarily as dense knots or filaments oriented on either side of the jet in an alternating pattern (see, e.g., Fig. 10*c* at $x \sim 100R_{jt}$). Strong cooling effects are clearly observable in these simulations, especially for the jet with MB cooling, where the cooling rate for jet material is very high. The strong cooling in this case leads to condensation in the region in which the amplitude of the perturbation becomes significant. The most prominent of these structures that are at an axial distance less than or on the order of $100R_{jt}$ have an observed wavelength $\lambda \approx 17.3R_{jt}$ (Ad), $13.4R_{jt}$ (DM), and $14.2R_{jt}$ (MB). The linear analysis in Paper I shows that the first asymmetric body mode wave on the adiabatic jet would respond to this low-frequency perturbation with a wavelength of $21R_{jt}$, not much longer than that observed in the simulation. However, the first asymmetric body wave on the DM and MB cooling jets is damped at this low frequency. However, we note that the observed wavelengths fall very close to the longest wavelength $15.3R_{jt}$ on the DM cooling jet and $14.7R_{jt}$ on the MB cooling jet at which the first asymmetric body wave is unstable. Thus, we identify these internal structures with asymmetric body waves excited by the low-frequency perturbation.

3.2.3. *Disruption of the Jet*

Once the amplitude of a surface wave at the maximally growing wavelength becomes on the order of the jet radius, the jet can no longer remain collimated and will disrupt. For wavelengths longer than the maximally growing wavelength, the amplitude can be correspondingly larger before the jet disrupts. This result is a consequence of the fact that disruption occurs when transverse motions in the reference frame of the wave approach the sound speed in the jet fluid. The distance a jet propagates before disruption depends on its Mach number (higher Mach number jets propagate farther), on the growth rate of the surface wave at the perturbation frequency (higher growth rates produce quicker disruption), on the initial perturbation amplitude, and on the perturbation wavelength relative to the maximally growing wavelength. Disruption of the jet by the surface wave can be observed in each of the jets shown in Figures 6 and 10 and also in the DM cooling jet in Figure 9. Beyond the point of disruption, the jet and ambient gas are strongly mixed, and shocked jet and ambient material are compressed into dense knots.

The results of an extensive series of simulations at different perturbation frequencies and amplitudes indicate that jet disruption can be summarized as follows:

1. For very low frequency perturbations, jet disruption occurs via the surface wave or low-order body modes, even though both have low growth rates.
2. For intermediate-frequency perturbations, the jets are disrupted by the surface wave.
3. For high-frequency perturbations, cooling jets are disrupted by strong body waves. On the other hand, body modes in the adiabatic jet tend to saturate at a finite amplitude and do not disrupt the jet

3.2.4. *Formation of Knots*

A common feature observed in our simulations of cooling jets is the formation of dense knots of cool gas. We find there are two separate mechanisms by which such knots can be formed. The first is the sweeping up of ambient gas by either (1) large-amplitude oscillations of the jet caused by growth of the surface wave or (2) disruption of the jet. This mechanism is similar in principle to the processes that form knots at the working surface of propagating protostellar jets (see, e.g., Blondin, Fryxell, & Königl 1990; Stone & Norman 1994). The second mechanism is associated with the growth of body waves internal to the jet or in the linear growth phase of the sinusoidal surface wave that is accompanied by waves internal to the jet. In the nonlinear regime, these waves form shocks in the jet, and strong cooling in the postshock gas can result in condensation of dense knots. Note that in this case, the knots are composed entirely of cooled jet material and are contained within the jet, whereas in the former process, the knots are composed of both jet and swept up ambient material.

The Mach 5 cooling jets shown in Figure 10 provide evidence for the formation of knots via both the first and second mechanism. Growth of the sinusoidal oscillation results in large-amplitude displacement of the jet that then sweeps up ambient gas. When enough gas has accumulated, the jet starts to break up, and mixing of jet and ambient material follows. As a result of strong cooling, dense knots are formed in the mixing region (especially for MB cooling, where jet material has a much higher cooling rate). This affect is seen quite strongly in the Mach 20 DM cooling jet shown in Figure 9 as well. Both of the Mach 5 cooling jets and the Mach 20 DM cooling jet in these figures demonstrate knot formation via the second mechanisms as well. In these jets, we observe strong oblique internal waves associated with the first asymmetric body wave. The strength of the internal wave grows rapidly, and dense knots are formed inside the jet (particularly in the MB cooling jet), but the jets still remain well collimated. The Mach 5 cooling jets shown in Figures 7 and 8 also provide evidence for knot formation via the second mechanism. These jets also contain strong oblique internal waves, and dense knots are formed inside the jet before the overall sinusoidal oscillation reaches sufficiently large amplitude to disrupt the collimated outflow.

Note that the excitation state of gas in knots should be different depending on whether the knot material came from jet fluid or from a mixture of jet and ambient fluid. Owing to the very high growth rate of the surface wave for the DM cooling jet, we expect knots to contain a mixture of jet and ambient fluid as the jet disrupts very quickly. In most of the cases in which perturbations have intermediate frequencies, we expect that both of the mechanisms can be responsible for the formation of dense knots.

3.2.5. *Mixing and Entrainment*

In the nonlinear regime, K-H instabilities can strongly alter the structure of a collimated jet and lead to mixing and

entrainment of ambient gas. Such mixing transfers momentum from the high-velocity jet material to the ambient medium, accelerating the latter and increasing the mass of outflowing material. In the case of protostellar jets, entrainment of high-velocity jet material into the ambient medium has been suggested as a mechanism for driving low-velocity molecular bipolar outflows, either by steady entrainment due to turbulence in a mixing layer between the jet and ambient gas (Stahler 1994) or by prompt entrainment in the "turbulent wakes" behind multiple bow shocks (Raga & Cabrit 1993). In our simulations, we can use the Lagrangian tracer or "color" variable C of the fluid to study quantitatively the mixing of the jet and ambient gases.

In Figure 11*a*, we plot the entrainment volume V_ϵ (defined as the volume of fluid that has $C > \epsilon$, where $0 < \epsilon < 1$ (see, e.g., Loken et al. 1996), while in Figure 11*b*, we plot the entrained mass M_δ (defined as the mass of fluid with $v_x > \delta$, where v_x is the axial component of velocity (see, e.g., Loken et al. 1996; Bassett & Woodward 1995) as a function of position x along the jet. Both plots are constructed at late dynamical times ($t = 200\tau$, or 2.5 grid crossing times) for a Mach 5 jet computed with DM cooling and driven at a frequency of $\omega R_{\rm jt}/u = 0.1$ (this is the jet shown in Fig. 10*b*). The jet structure has reached a quasi steady state by this time, and we average the axial profiles of both variables over a short time interval to remove the influence of discrete knots. The plots in Figure 11 illustrate the spatial variation in entrainment along the length of the jet driven by the growth of K-H modes.

As expected, we find that little mixing occurs near the jet nozzle, i.e., inside $x = 100R_{\rm jt}$, where the waves are still in the linear regime. Beyond $100R_{\rm jt}$, Figure 11*a* demonstrates that the entrainment volume V_ϵ shows a rapid increase for every value of ϵ, which inidcates that strong mixing is occurring. We find that mixing of the ambient gas starts where the perturbation reaches significant amplitude and then grows exponentially with the amplitude of the perturbation. This spatial growth of the mixing fraction appears to be in agreement with the results of Bodo et al. (1995). The spikes in the entrainment volume occurring at $x \approx 160$ and $x \approx 180$ are due to discrete knots of fluid shed by the jet beam during the initial growth of the instability; they are not part of the main beam at late times (see Fig. 10*b*). The entrained mass M_δ plotted in Figure 11*b* drops for $v_x > 5$ (the initial jet velocity), while M_δ increases for all values of $v_x < 5$, and this clearly indicates mass is being entrained and accelerated by the jet. For very small values of v_x (e.g., $v_x < 0.1$), we find M_δ begins to increase within $50R_{\rm jt}$ of the nozzle, even before the jet disrupts and mixes significantly (i.e., before V_ϵ begins to increase). However, Figure 10*b* shows that in this region, strong shock spurs are driven into the ambient gas by the sinusoidal distortion of the jet. These shock spurs result in acceleration of the ambient gas. Although most previous discussions of the entrainment and acceleration of ambient gas along a jet beam have focused on turbulence either in a mixing layer, or in the turbulent "wake" of internal bow shocks in pulsed jets, our simulations show that shock trains in the ambient gas can result in acceleration of ambient gas. These shock trains may be produced by the K-H instability, as our simulations demonstrate, or they may be the wings of internal bow shocks produced by pulsing the jet. In fact, all of our simulations of the asymmetric mode of the K-H instability show the formation of shock spurs, which accelerates the ambient gas to some degree. Moreover, we note that neither our hydrodynamical simulations of these shock spurs nor simulations of the wings of internal bow shocks (Stone & Norman 1994; Biro & Raga 1994) show evidence for "turbulent wakes."

On the other hand, we find that strong entrainment of ambient gas does not occur until the jet disrupts. Moreover, since the jets are not always disrupted by the asymmetric modes, not all of our simulations show strong mixing and entrainment of ambient gas, e.g., the Mach 5 cooling jets shown in Figure 7. However, our two-dimensional simulations cannot capture all modes of the K-H instability present in three dimensions; e.g., we lose the higher order fluting modes. It is possible, therefore, that the mixing rate in the nonlinear regime will be higher in three-dimensional simulations of unstable jets. In addition, very high resolution two-dimensional simulations of the temporal growth of K-H modes in low Mach number adiabatic jets (Bassett & Woodward 1995) indicate that high-order modes can significantly increase the mixing rate, which suggests that numerical resolution may limit our results. However, it

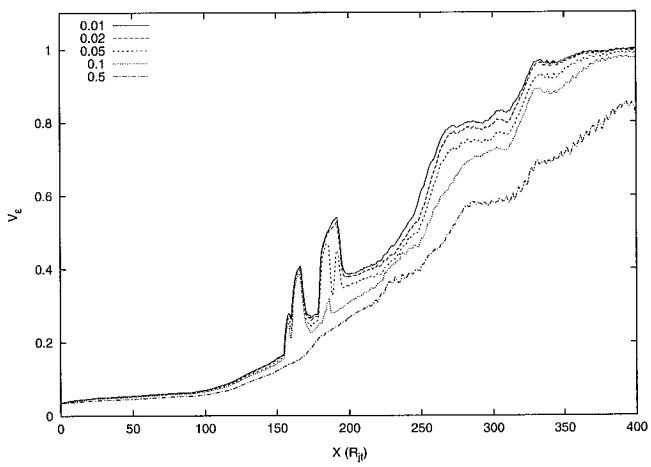

FIG. 11*a*

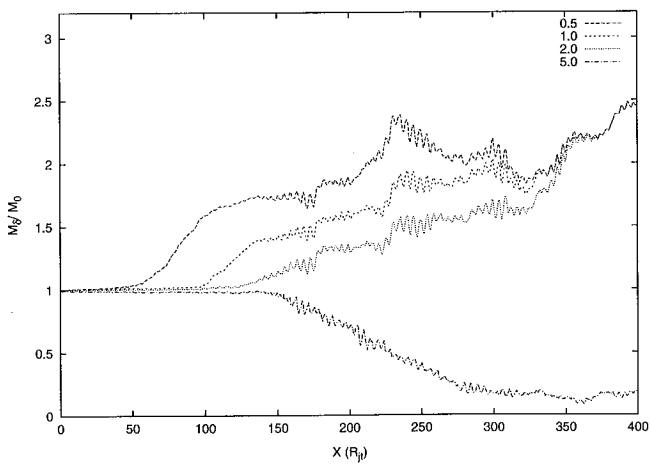

FIG. 11*b*

FIG. 11.—(*a*) Entrainment volume V_ϵ vs. axial position at late times in a Mach 5 DM cooling jet perturbed at a frequency of $\omega R_{\rm jt}/u = 0.1$ (cf. Fig. 10*b*). Curves shown are for $\epsilon = 0.01, 0.02, 0.05, 0.1$, and 0.5. (*b*) Entrained mass M_δ vs. axial position for the same jet. Curves shown are for $\delta = 0.5, 1, 2$, and 5.

is not clear if these results apply to the spatial growth of modes in high Mach number jets as studied here.

4. COMPARISON TO PROTOSTELLAR JETS

Although we have studied the dynamical effect of a cooling curve appropriate to photoionized gas of low metallicity (appropriate for jets from active galactic nuclei such as Seyferts) in addition to a cooling curve more appropriate to protostellar jets, the most detailed observations of optical jets collected to date have been of protostellar systems. Thus, in this paper, we focused on simulations that use parameter values (see § 2.3) representative of protostellar rather than Seyfert jets. For example, we have studied overdense ($n_{\rm jt}/n_{\rm ex} = 10$) jets, whereas jets from active galactic nuclei are usually thought to be density matched or underdense with respect to their surroundings. While detailed modeling of Seyfert jets is a fruitful direction for future work, in this section we focus on a comparison between our numerical simulations and observations of protostellar jets.

There are a number of striking similarities between the structures we observe in our simulations and the morphology of observed systems. For example, the low-amplitude oscillations, the formation of asymmetric knots in the jet, and the shock spurs driven into the ambient gas resulting from the growth of the body waves (see Fig. 7) are all reminiscent of features seen in *HST* observations of jets such as HH 34 and HH 111 (Reipurth et al. 1997). *HST* observations of HH 47 reported by Heathcote et al. (1996) indicate a complex structure, with the jet undergoing several bends before terminating at the Mach disk and bow shock structure HH 47A. Interestingly, the jet structure seen in the DM cooling jet simulation shown in Figure 9 strongly resembles the observations of HH 47. Fabry-Perot observations of the kinematics of HH 47 (Hartigan et al. 1993) show that the fastest moving jet material is confined to the core of the beam, with slower moving material forming a thick sheath around the jet. Raymond et al. (1994) have compared the kinematics of the HH 47 jet to models based on both viscous entrainment and acceleration due to mass ejected from the beam by internal bow shocks. In this paper, we have found that shock spurs produced by low-amplitude kinks in the beam that result from the K-H instability may be another mechanism for accelerating ambient gas in a sheath surrounding the jet beam. Our simulations indicate that it is not necessary for protostellar jets to be "precessing" through a large angle to generate kinks or wiggles. Instead, small-amplitude linear waves introduced into the jet via small perturbations can excite K-H instabilities to produce similar structures.

There is strong evidence, based on kinematic data and the bow shock–like shape, that many internal knots in protostellar jets are due to pulsing. At the same time, many sources show low-amplitude wiggles and asymmetric knots (as well as internal bow shocks) that are difficult to explain by pulsing alone. Such jets may best be modeled by the growth of instabilities in a pulsed jet, a problem we have not considered here.

The peak in the growth rate for sinusoidal surface waves on adiabatic and jets with a MacDonald & Bailey cooling curve is at a resonant frequency of $\omega R_{\rm jt}/a_{\rm ex} \approx 1.5$. For jets with a Dalgarno & McCray cooling curve, this frequency is also about the highest frequency to which the entire jet can respond dynamically. A similar result is found for helical twisting in three dimensions. For parameters typical of protostellar jets, the frequency $\omega R_{\rm jt}/a_{\rm ex} \approx 1.5$ corresponds to perturbations with $\omega R_{\rm jt}/u \approx 0.1$ and a period of approximately 200 yr. However, if the jet is driven from the inner regions of the accretion disk ($r \leq 1$ AU), the characteristic time for perturbations (of order an orbital time) are much shorter. Our simulations show that jets that are driven at frequencies much higher than the resonant frequency cannot respond dynamically with a short wavelength corresponding to the high frequency, although the jet may show irregular oscillation (see the DM cooling jet in Fig. 6) and form internal structures via internal waves (see Fig. 7). This result is consistent with the observation that most protostellar jets are remarkably straight and usually show no evidence of large scale sinusoidal oscillations (which in three dimensions would result from helical twisting of the jet) leading to disruption of the type shown in Figure 6.

Of course, observed jets may contain structures associated with three-dimensional modes of the K-H instability that cannot be captured in our two-dimensional simulations. We will report on the comparison of three-dimensional simulations of K-H unstable protostellar jets with *HST* observations in a future communication.

5. CONCLUSIONS

In this, the second of two papers, we have studied the asymmetric modes of the K-H instability in jets in which optically thin radiative cooling is dynamically important, such as the jets associated with protostellar outflows and Seyfert galaxies. In Paper I, we presented solutions to the dispersion relation in the linear regime for K-H modes in a cooling jet over a wide range of perturbation frequencies. Our results indicated that the linear growth rates of waves in a cooling jet are substantially different from those of an adiabatic jet. Depending on the details of the cooling function adopted, the growth rate of waves could be either enhanced or reduced relative to those on the adiabatic jet. In this paper, we have continued this analysis by using time-dependent hydrodynamical simulations to follow the growth of unstable waves into the nonlinear regime.

As a consistency check, we first compared the linear growth rates of waves in our numerical simulations with predictions from the analytical results of Paper I. We found excellent agreement between the measured and predicted growth rates over a wide range of frequencies. This observation serves both as a code test, and a confirmation of the results of Paper I.

In the nonlinear regime, we observe a variety of interesting effects. Growth accompanying low-frequency and long-wavelength perturbations can dominate the structure of the jet at late times, producing large-amplitude sinusoidal oscillations of the jet beam. Once the amplitude of the oscillations exceeds several jet radii, the jet is disrupted. On the other hand, higher frequency perturbations can excite body waves that result in the formation of internal sinusoidal structures. Strong internal shocks produced by these body waves can form a pattern of dense knots that are staggered asymmetrically along the length of the jet. We find that internal shocks produced by relatively short wavelength body waves can coexist on a jet with a much longer wavelength, slowly growing, sinusoidal oscillation of the entire jet. We also find that small-amplitude oscillations of the jet associated with a growing sinusoidal surface or with a strong body wave can drive shock spurs into the ambient gas, which leads to an alternating pattern of knots and

shock spurs. These shock spurs can accelerate the ambient gas without mixing it with the jet fluid. On the other hand, disruption of the jet by the K-H instability produces strong mixing and entrainment of ambient gas and the formation of dense knots of shocked ambient gas swept up by jet material.

Structures observed in our simulations such as low-amplitude wiggles in the jet, dense knots formed asymmetrically with respect to the center of the jet, and an alternating pattern of shock spurs driven into the ambient gas are all reminiscent of high-resolution observations of protostellar jets. On the other hand, for a typical protostellar jet, dynamical periods associated with the inner ($r < 1$ AU) regions of an accretion disk are much less than the period of perturbations to which the entire jet can respond dynamically (which is about 200 yr). We therefore expect protostellar jets to be dominated by the growth of body waves and internal asymmetric structures rather than the surface waves. It is the surface waves that lead to large-scale apparent sinusoidal oscillation (resulting from helical twisting) of the entire jet and that would result in disruption of the jet at nonlinear amplitudes, features that typically are not observed in real systems.

In this initial study, we have confined our simulations to the two-dimensional slab jet. We will report on the linear stability analysis and hydrodynamic simulations of three-dimensional cooling jets in a future communication.

This research is supported by the NASA ATP through grant NAG-4202 to the University of Maryland and by the NSF through grant AST 93-18397 to the University of Alabama.

REFERENCES

Bassett, G. M., & Woodward, P. R. 1995, ApJ, 441, 582
Birkinshaw, M. 1991, in Beams and Jets in Astrophysics, ed. P. Hughes (Cambridge: Cambridge Univ. Press), 278
Biro, S., & Raga, A. C. 1994, ApJ, 434, 221
Biro, S., Raga, A. C., & Cantó, J. 1995, MNRAS, 275, 557
Blondin, J. M., Fryxell, B. A., & Königl, A. 1990, ApJ, 360, 370
Bodo, G., Massaglia, S., Ferrari, A., & Trussoni, E. 1994, A&A, 283, 655
Bodo, G., Massaglia, S., Rossi, P., Rosner, R., Malagoli, A., & Ferrari, A. 1995, A&A, 303, 281
Bryan, G. L., Norman, M. L., Stone, J. M., Cen, R., & Ostriker, J. P. 1995, Comput. Phys. Comm., 89, 149
Bührke, T., Mundt, R., & Ray, T. P. 1988, A&A, 200, 99 (BMR)
Cecil, G., Wilson, A. S., & Tully, R. B. 1992, ApJ, 390, 365
Clarke, D. A. 1993, in Lecture Notes in Physics 421, Jets in Extragalactic Radio Sources, ed. H.-J. Röser & K. Meisenheimer (Berlin: Springer), 243
Dalgarno, A., & McCray, R. A. 1972, ARA&A, 10, 375 (DM)
Edwards, S., Ray, T. P., & Mundt, R. 1993, in Protostars and Planets III, ed. E. Levy & J. Lunine (Tucson: Univ. of Arizona Press), 567
Eislöffel, J., & Mundt, R. 1994, A&A, 284, 530
Ferrari, A., Trussoni, E., & Zaninetti, L. 1981, MNRAS, 196, 1051
Gouviea dal Pino, E. M., & Benz, W. 1994, ApJ, 435, 261
Hardee, P. E. 1987, ApJ, 313, 607
Hardee, P. E., & Norman, M. L. 1988, ApJ, 334, 70
Hardee, P. E., Norman, M. L., & Clarke, D. A. 1994, ApJ, 424,126
Hardee, P. E., & Stone, J. M. 1997, ApJ, 483, 121 (Paper I)
Hartigan, P., Morse, J. A., Heathcote, S., & Cecil, G. 1993, ApJ, 414, L121
Hartigan, P., & Raymond, J. 1993, ApJ, 409, 705
Heathcote, S., Morse, J., Hartigan, P., Reipurth, B., Schwartz, R. D., Bally, J., & Stone, J. M. 1996, AJ, 112, 1141
Hunter, J. H., & Whitaker, R. W. 1989, ApJS, 71, 777
Loken, C., Burns, J., Bryan, G., & Norman, M. L. 1996, in ASP Conf. Proc. 100, Energy Transport in Extragalactic Radio Sources and Quasars, ed. P. Hardee, A. Bridle, & A. Zensus (San Francisco: ASP), 267
MacDonald, J., & Bailey, M. E. 1981, MNRAS, 197, 995 (MB)
Massaglia, S., Trussoni, E., Bodo, G., Rossi, P., & Ferrari, A. 1992, A&A, 260, 243
Nagar, N., Vogel, S., & Stone, J. M. 1996, ApJ, submitted
Norman, M. L., & Balsara, D. S. 1993, in Lecture Notes in Physics, 421, Jets in Extragalactic Radio Sources, ed. H.-J. Röser & K. Meisenheimer (Berlin: Springer), 229
Raga, A. C., & Biro, S. 1993, MNRAS, 264, 758
Raga, A. C., & Cabrit, S. 1993, A&A, 278, 267
Raga, A. C., & Cantó, J. 1996, MNRAS, 280, 567
Raga, A. C., Cantó, J., & Biro, S. 1993, MNRAS, 260, 163
Raga, A. C., & Kofman, L. 1992, ApJ, 386, 222
Ray, T. P. 1996, in Proc. of the NATO ASI on Solar and Astrophysical MHD Flows, ed. K. Tsinganos (Dordrecht: Kluwer), in press
Ray, T. P., et al. 1997, in preparation
Raymond, J. C., Morse, J. A., Hartigan, P., Curiel, S., & Heathcote, S. 1994, ApJ, 434, 232
Reipurth, B., et al. 1997, in preparation
Reipurth, B., & Cernicharo, J. 1995, Rev. Mexicana Astron. Astrofis. Ser. Conf., 1, 43
Reipurth, B., Raga, A. C., & Heathcote, S. 1996, preprint
Stahler, S. W. 1994, ApJ, 422, 616.
Stapelfeldt, K., et al. 1997, in preparation
Stone, J. M., & Norman, M. L. 1993a, ApJ, 413, 198
———. 1993b, ApJ, 413, 210
———. 1994, ApJ, 420, 237
Wilson, M. J. 1988, in Lecture Notes in Physics, 327, Hot Spots in Extragalactic Radio Sources, ed. K. Meisenheimer & H.-J. Röser (Berlin: Springer), 215
Zhao, J. H., Burns, J. O., Hardee, P. E., & Norman, M. L. 1992, ApJ, 387, 69

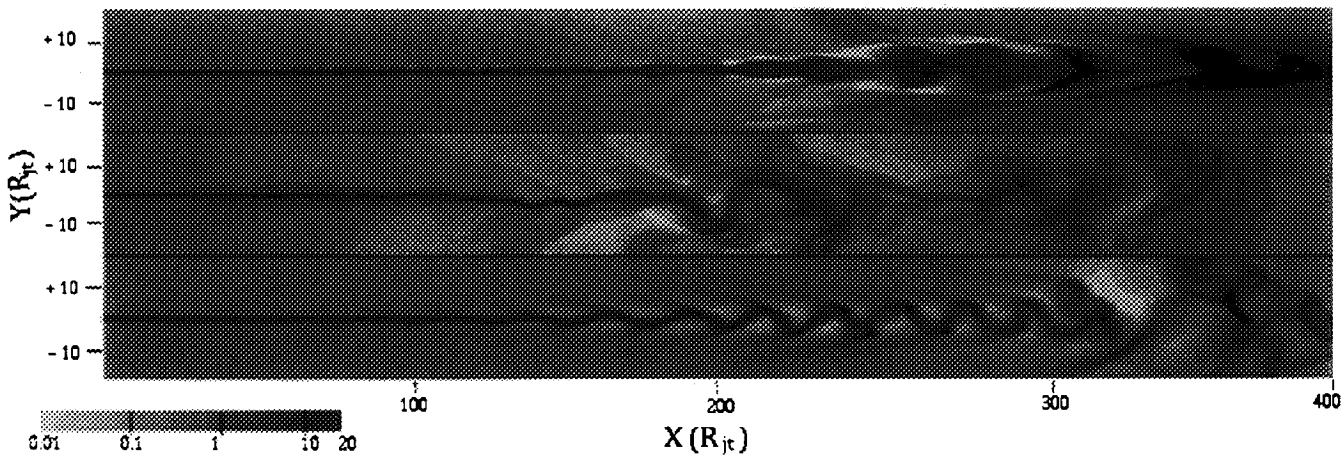

FIG. 6.—Gray-scale images of the logarithm of the density for a Mach 5 adiabatic (*top*), DM cooling (*middle*), and MB cooling (*bottom*) jet perturbed with a frequency $\omega R_{jt}/u = 1.0$ at the nozzle. Note the MB cooling jet shows a regular sinusoidal pattern indicating the dominance of a resonance frequency as expected from the dispersion relation of the surface wave.

STONE, XU, & HARDEE (see 483, 142)

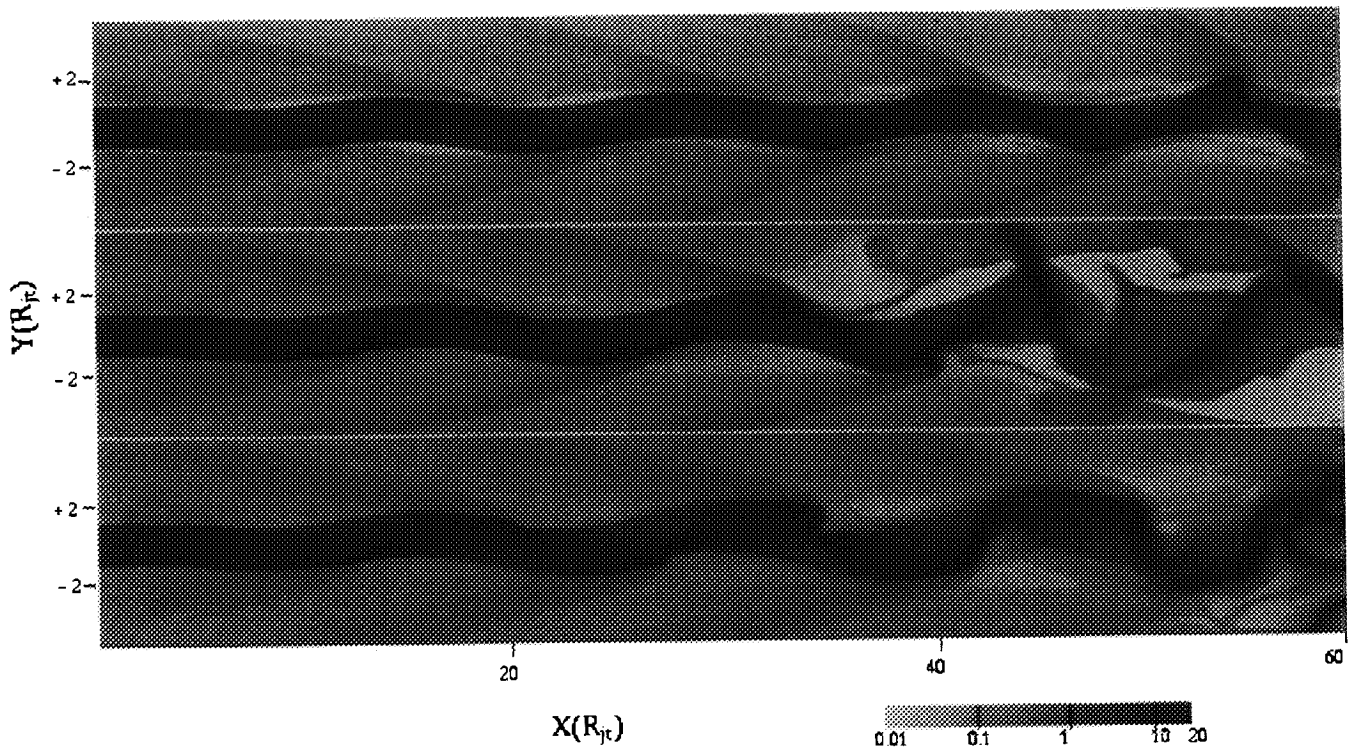

FIG. 7.—Gray-scale images of the logarithm of the density for a Mach 5 adiabatic (*top*), DM cooling (*middle*), and MB cooling (*bottom*) jet perturbed with a frequency $\omega R_{jt}/u = 0.4$ at the nozzle. Dense knots and filaments are formed in a sinusoidal pattern owing to the nonlinear evolution of the surface wave. In the cooling jets (*bottom two panels*), these knots are R-T unstable and fragment at late times.

STONE, XU, & HARDEE (see 483, 142)

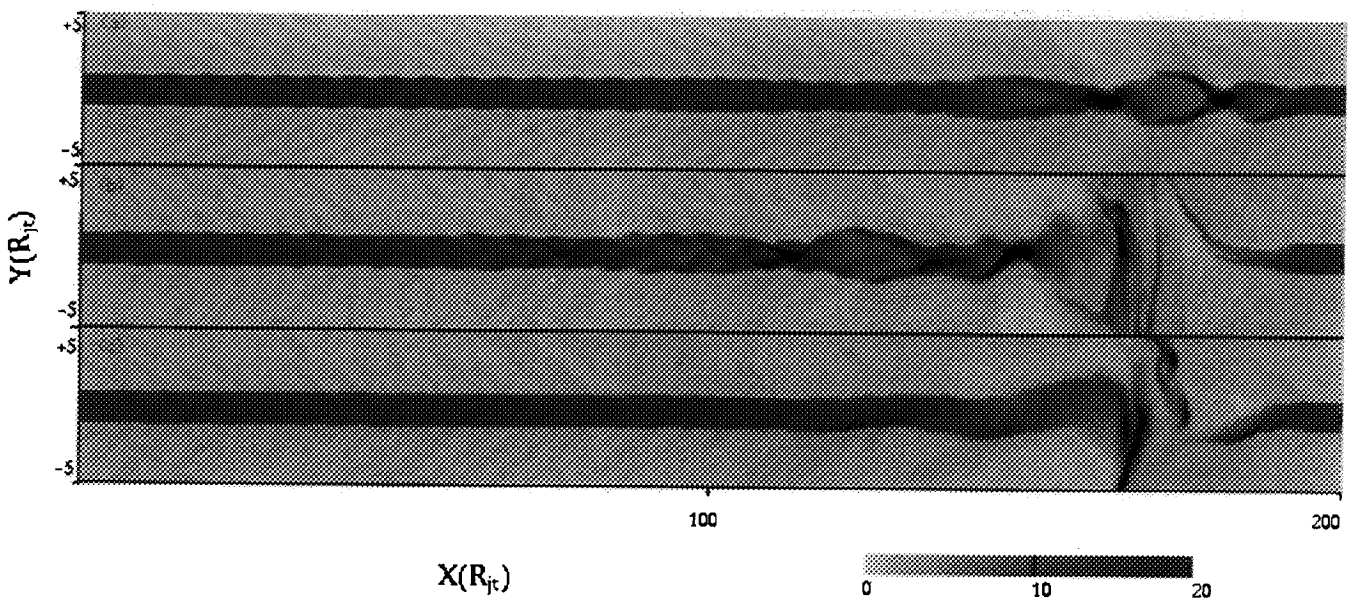

FIG. 8.—Gray-scale images of the density for high-resolution simulations of a Mach 5 adiabatic (*top*), DM cooling (*middle*), and MB cooling (*bottom*) jet perturbed with a frequency $\omega R_{jt}/u = 1.0$ at the nozzle, showing the growth and interaction of body modes and surface waves.

STONE, XU, & HARDEE (see 483, 143)

PLATE 6

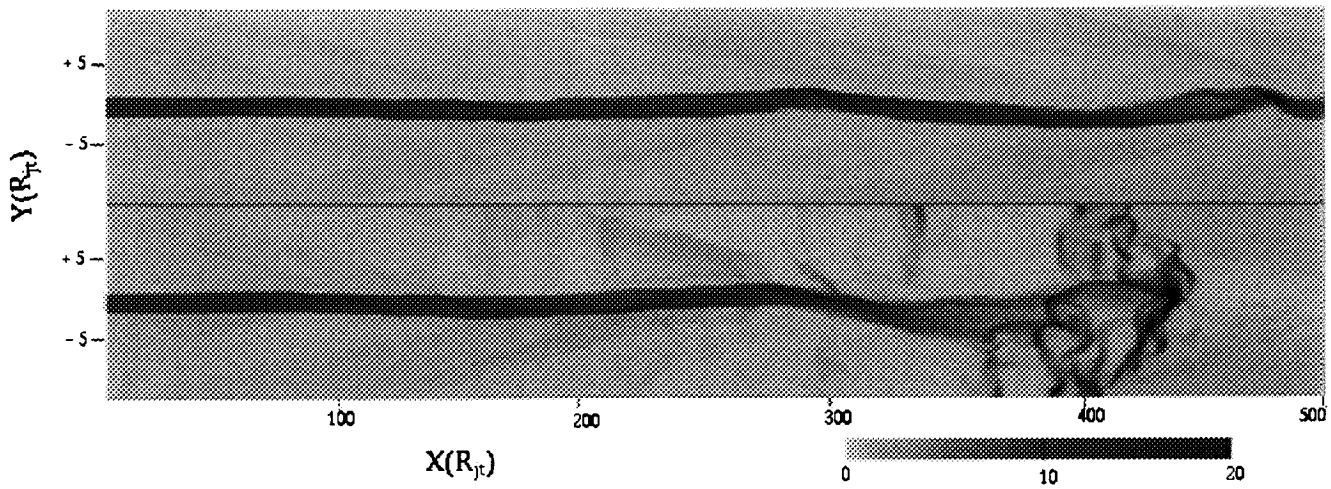

FIG. 9.—Gray-scale images of the density for a Mach 20 adiabatic (*top*) and DM cooling (*bottom*) jet perturbed with a frequency $\omega R_{jt}/u = 0.025$ at the nozzle. Internal structure produced by the body modes is evident.

STONE, XU, & HARDEE (see 483, 143)

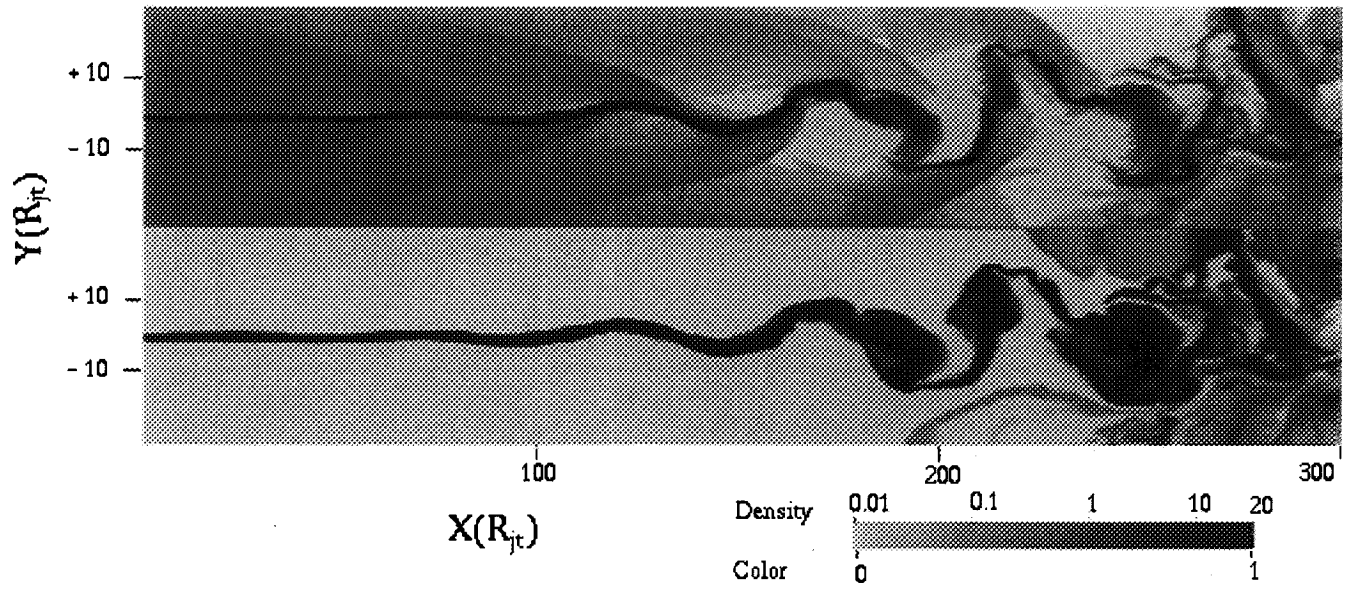

FIG. 10*a*

FIG. 10.—Gray-scale images of the logarithm of the density and the color variable C for a Mach 5 (*a*) adiabatic, (*b*) DM cooling, and (*c*) MB cooling jet perturbed with a frequency $\omega R_{j0}/u = 0.1$ at the nozzle. Strong mixing is evident once the jet disrupts.

STONE, XU, & HARDEE (see 483, 143)

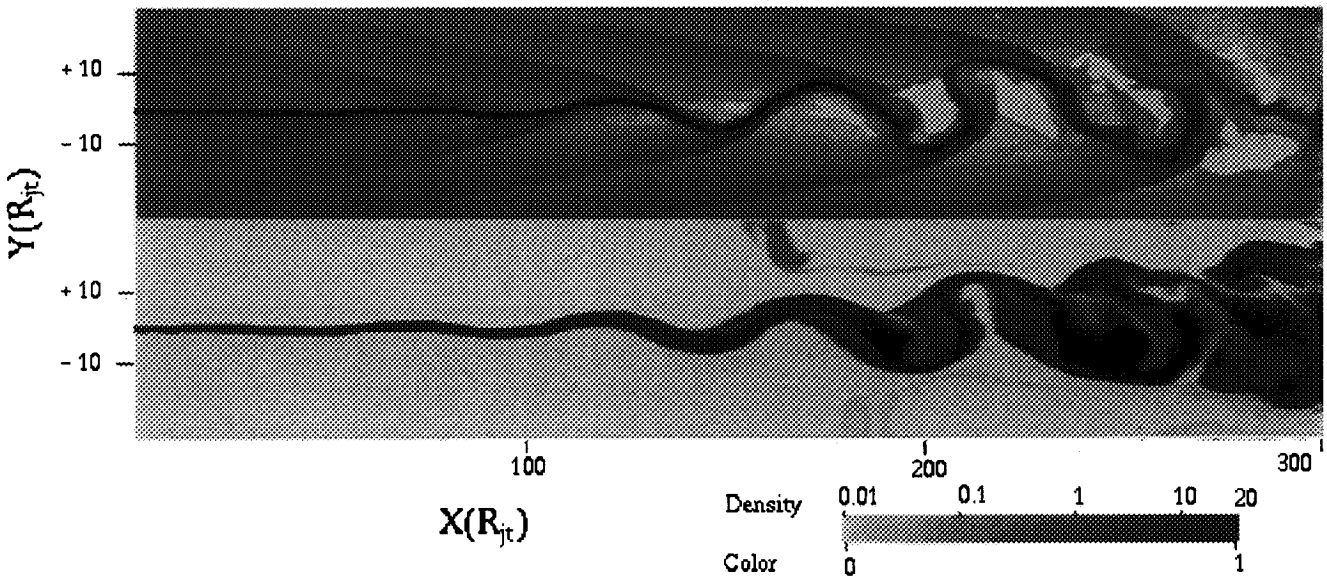

FIG. 10*b*

STONE, XU, & HARDEE (see 483, 143)

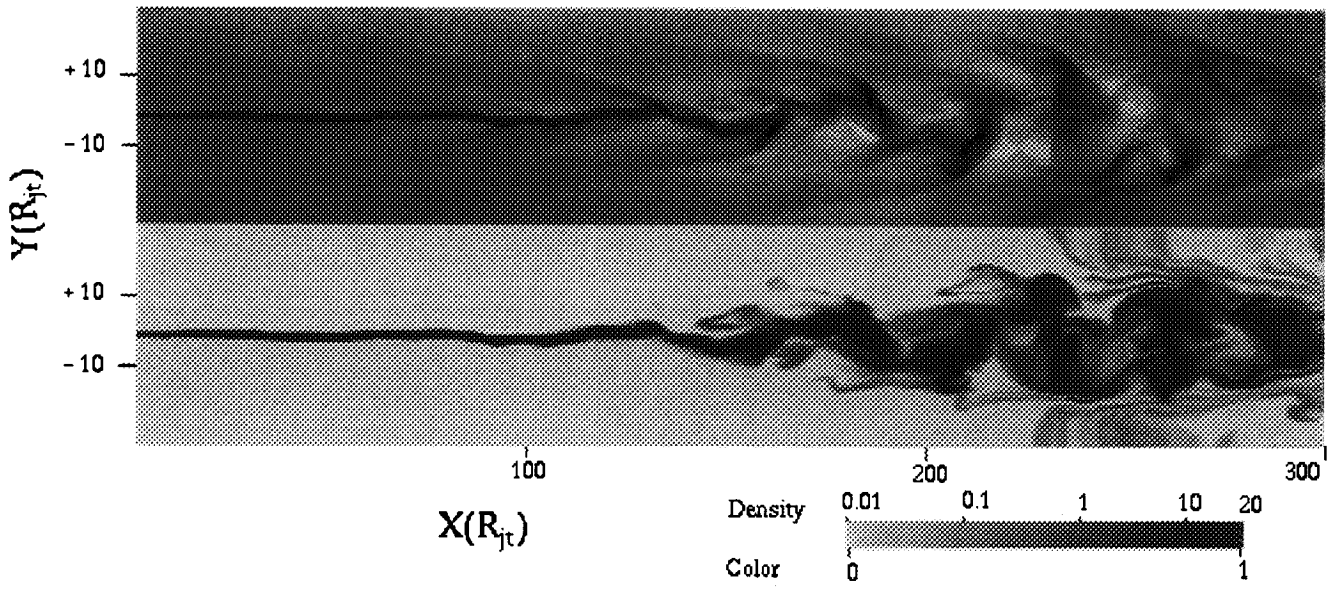

FIG. 10*c*

STONE, XU, & HARDEE (see 483, 143)